Multimodal Surface Instabilities in Curved Film–Substrate Structures

Ruike Zhao
Soft Active Materials Laboratory,
Department of Mechanical Engineering,
Massachusetts Institute of Technology,
Cambridge, MA 02139

Xuanhe Zhao
Soft Active Materials Laboratory,
Department of Mechanical Engineering,
Massachusetts Institute of Technology,
Cambridge, MA 02139;
Department of Civil and Environmental Engineering,
Massachusetts Institute of Technology,
Cambridge, MA 02139
e-mail: zhaox@mit.edu

Structures of thin films bonded on thick substrates are abundant in biological systems and engineering applications. Mismatch strains due to expansion of the films or shrinkage of the substrates can induce various modes of surface instabilities such as wrinkling, creasing, period doubling, folding, ridging, and delamination. In many cases, the film–substrate structures are not flat but curved. While it is known that the surface instabilities can be controlled by film–substrate mechanical properties, adhesion and mismatch strain, effects of the structures' curvature on multiple modes of instabilities have not been well understood. In this paper, we provide a systematic study on the formation of multimodal surface instabilities on film–substrate tubular structures with different curvatures through combined theoretical analysis and numerical simulation. We first introduce a method to quantitatively categorize various instability patterns by analyzing their wave frequencies using fast Fourier transform (FFT). We show that the curved film–substrate structures delay the critical mismatch strain for wrinkling when the system modulus ratio between the film and substrate is relatively large, compared with flat ones with otherwise the same properties. In addition, concave structures promote creasing and folding, and suppress ridging. On the contrary, convex structures promote ridging and suppress creasing and folding. A set of phase diagrams are calculated to guide future design and analysis of multimodal surface instabilities in curved structures.
[DOI: 10.1115/1.4036940]

Keywords: instability, curvature, film–substrate structure, morphogenesis

1 Introduction

Structures of thin films bonded on thick substrates are abundant in biological systems and engineering applications; examples include various biological tissues [1,2], flexible electronics and wearable devices [3–6], strain-controlled superhydrophobicity [7,8], and self-assembled patterns [9]. Mismatch strains due to expansion of the films or shrinkage of the substrates can induce various modes of surface instabilities including wrinkling [10–15], creasing [16–20], period doubling [21–23], folding, ridging [24,25], delamination [26], 2D-buckling [27–30], 3D-buckling [31–33], and hierarchical wrinkles [34–36]. Some examples of surface instability patterns have been given in Fig. 1(*a*). Over last few decades, various modes of instabilities in the film–substrate structures have been studied individually [23,25,37,38] and systematically by categorizing them on phase diagrams [39–43]. It is well known that these instabilities can be controlled by mechanical properties such as rigidities of films and substrates, the adhesion energies between them, and their mismatch strains or compressive strains applied on the structures.

Many film–substrate structures found in nature, biological systems, and engineering applications are not flat but curved, although previous studies have been focused on flat cases. For example, Fig. 1(*b*) illustrates different surface instability patterns on concave film–substrate structures. From left to right (Fig. 1(*b*)), mucosa-growth induced creases are seen in colon; the anatomic ductus deferens in male reproductive system shows ridges on surface; muscular arteries manifest doubling patterns along the lamina; and wrinkling patterns are observed on the surface of bronchus lumen. Film–substrate structures with convex surface are commonly seen in plants, as shown in Fig. 1(*c*). From left to right, a bitter melon shows creases on its surface; cactus develops surface ridges; a tree stump reveals irregular doubling patterns on its bark; and a cereus presents uniform wrinkling on its skin. Other surface patterns on curved biological structures that have drawn much attention in the biochemistry and biomedical fields include morphological development of brain [44,45], growth-induced creases and folds in tubular tissues [46,47], crumpled gut surfaces [48–50], deformation of cell-culture substrates [51–54], and morphological evolution of tumor growth [55–58]. In engineering, curved film–substrate structures have been widely used in design of flexible and stretchable electronics [3,59], active detachment of biofouling [60–62], and control of aerodynamic drag [63,64].

A few theoretical and computational models have been developed to investigate the morphological instabilities and analyze the bifurcation conditions on curved film–substrate such as cylindrical [65–68] and spheroidal structures [9,69–72]. While previous studies have been focused on individual mode of instability such as wrinkle, crease, and fold, the effects of the structures' curvature on multiple modes of surface instabilities have not been well studied or understood. In this paper, we provide a systematic study on the formation of multimodal surface instabilities on film–substrate structures with different curvatures through both theoretical analysis and numerical simulation. We will focus our study on tubular film–substrate structures with both convex and concave curvatures (Fig. 1), as these structures appear abundantly in biological systems and engineering applications. We will apply the FFT method to quantitatively categorize various instability patterns on curved structures by analyzing their wave frequencies. Thereafter, we will develop a theoretical model to predict the critical mismatch strain and wavenumber of wrinkling instability on curved film–substrate structures, followed by finite element simulation of the formation of advanced modes of instabilities. We will show that the curved film–substrate structures can delay the critical mismatch strain for wrinkling for systems with relatively large film–substrate modulus ratio, compared with flat ones with otherwise the same properties. Furthermore, concave structures promote creasing and folding and suppress ridging, but convex

Contributed by the Applied Mechanics Division of ASME for publication in the Journal of Applied Mechanics. Manuscript received May 5, 2017; final manuscript received May 29, 2017; published online June 13, 2017. Editor: Yonggang Huang.

structures promote ridging and suppress creasing and folding. A set of phase diagrams will be calculated to guide future design and analysis of multimodal surface instabilities on curved structures.

The outline of this paper is as follows. Section 2 explains the definition of configurations and quantities in the problem. In Sec. 3, the FFT method is applied to quantitatively categorize the surface instability patterns. In Sec. 4, basic equations of continuum mechanics and incremental method in analyzing the deformation and instability of film–substrate structures are summarized. Section 5 presents the instability analysis to search for the critical mismatch strain and wavenumber for wrinkling on curved film–substrate structures. Section 6 accomplishes the finite element simulations of various modes of instabilities on film–substrate structures with various curvatures, mismatch strains, and modulus ratios. A set of phase diagrams for predicting various modes of instabilities in curved structures will be provided with the curvature's effects discussed. Final conclusions are made in Sec. 7.

2 Definition of States of the Film–Substrate Structures

Consider the plane-strain, incompressible deformation of a tubular film–substrate structure as illustrated in Fig. 2. The film can be bonded on the inner (Fig. 2(*a*)) or outer (Fig. 2(*d*)) surface of the tubular substrate, which gives the negative or positive curvature for the film–substrate structure, correspondingly. At the *reference state* (Figs. 2(*a*) and 2(*d*)), there is no mismatch strain between the film and the substrate, and a material point in the structure is denoted by its cylindrical coordinates (R, Θ, Z). The structure has the film radius A and interfacial radius B at the reference state (note that for negative-curvature structure, far-end of the substrate has radius C and $C \gg B$). The film thickness H at the reference state is defined as $H = |A - B|$. A mismatch strain may be applied to the system by either shrinking the substrate or expanding the film. In the current study, we will shrink the substrate to introduce the mismatch strain.

Under the mismatch strain, the film–substrate structure is deformed into the *current state*, and the material point (R, Θ, Z) moves to a new location (r, θ, z) at the current state in the cylindrical coordinate. The deformation of the structure may maintain homogenous (Figs. 2(*b*) and 2(*e*)) or become unstable (i.e., patterned in Figs. 2(*c*) and 2(*f*)) at the current state. The structure maintains tubular and patternless at the *current homogeneous state* with the film radius a and interfacial radius b. Based on the schematics in Fig. 2, the mismatch strain at the interface between the film and substrate at the current homogeneous state can be calculated as

$$\varepsilon_M = (B - b)/B \tag{1}$$

For the convenience of future discussion, we define the normalized curvature of the curved film–substrate structure as

$$\rho = (A - B)/b \tag{2}$$

A material point in the film has radius R at the reference state, and it moves to a new location at the current homogeneous state with radius r (Fig. 2). The circumferential compressive strain in the film at the current homogeneous state can be calculated as

$$\varepsilon_f = (R - r)/R \tag{3}$$

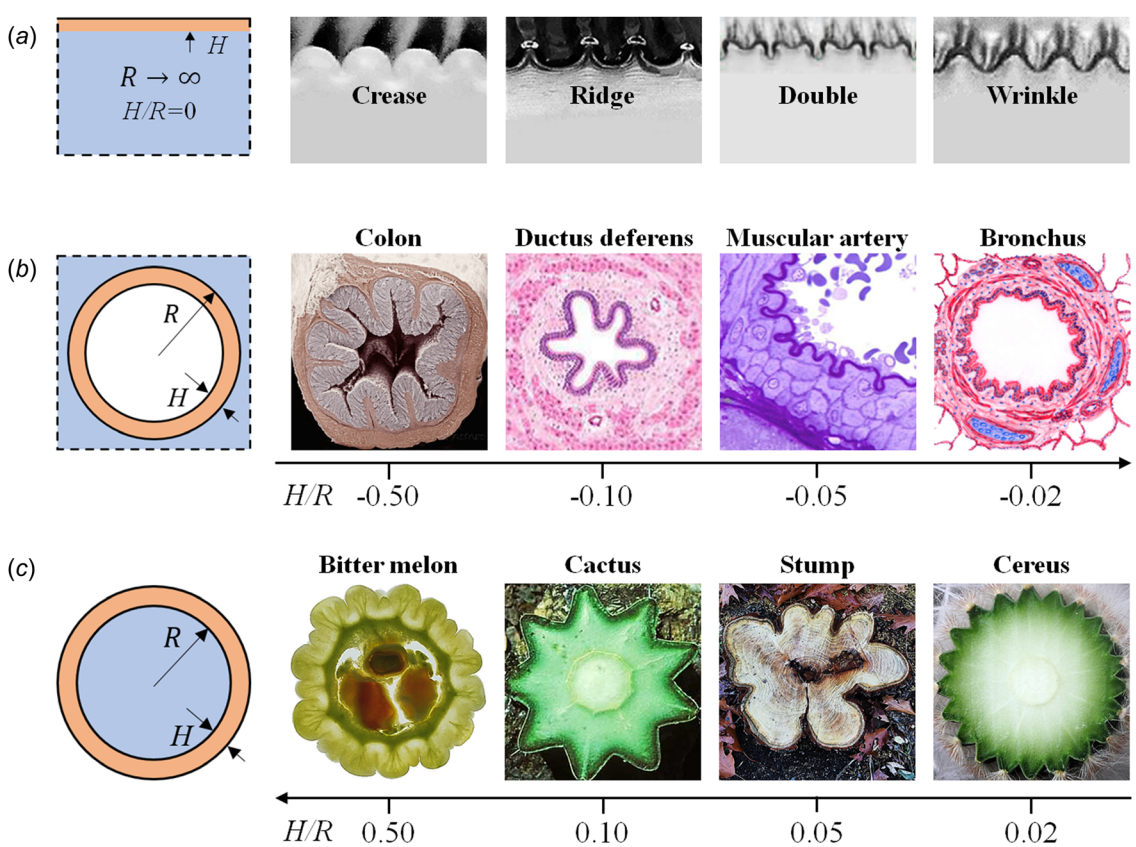

Fig. 1 Surface instabilities on curved film–substrate structures in nature and engineering applications. (*a*) Instabilities on flat structure (from left to right: crease, ridge, double, and wrinkle); (*b*) multimodal instabilities on concave structures (from left to right: cross section of colon, ductus deferens, muscular artery, and bronchus); and (*c*) multimodal instabilities on convex structures (from left to right: cross section of bitter melon, cactus, tree stump, and cereus).

Unlike in flat film–substrate systems, the compressive strain ε_f is not constant throughout the thickness of the film. From the incompressibility condition, we can derive the circumferential compressive strain in the film at current homogeneous state as a function of radius R and the applied mismatch strain ε_M at the interface

$$\varepsilon_f = 1 - \sqrt{1 + \left[(1-\varepsilon_M)^2 - 1\right]\left(\frac{B}{R}\right)^2} \tag{4}$$

where $A \le R \le B$ for concave structures and $B \le R \le A$ for convex structures. At the film–substrate interface, Eq. (4) can be reduced to $\varepsilon_f(R=B) = \varepsilon_M$. As R moves from the interface $(R=B)$ to film surface $(R=A)$, the compressive strain ε_f increases in the concave structures and decreases in the convex structures.

3 Quantitative Categorization of Surface Instability Patterns

While different modes of surface instabilities have different morphological patterns, categorizations of these surface instabilities patterns have mostly followed qualitative approaches. For example, the distinctions between wrinkles and advanced modes of instabilities including ridges, period doubles, and folds have only been qualitatively prescribed by previous researchers [15,16,24,37,39–43]. In addition, the introduction of curvatures in film–substrate systems will make the categorization of different modes of instabilities more complicated, as the curvature will affect the morphology of the same mode of instability (e.g., Figs. 3(*a*)–3(*c*)). As different modes of surface instabilities have different types of spatial periodicities, we propose to use the fast Fourier transformation method to quantitatively categorize various modes of surface instabilities by their frequency distribution. While this method has been used to analyze instability transition from wrinkle to crease of a flat graded material [37], here we further apply this method to distinguish various modes of instability patterns on curved surfaces. The frequency is in the space domain, and it is described by the wavelength of the instability pattern.

At the current patterned state, we record the coordinates of evenly distributed m points on the film surface (i.e., (r, θ, z) at $R=A$) from experiments or simulations. While the z coordinate is a constant due to plane-strain deformation, the r can be expressed as a function of θ, which ranges from 0 to 2π with equal interval of $2\pi/(m-1)$. The FFT computes the discrete Fourier transform (DFT) of the surface deformation by decomposing the deformation into components of different wave frequencies

$$y_{p+1} = \sum_{j=0}^{m-1} \left(e^{-\frac{2\pi i}{m}}\right)^{jp} r_{j+1} \tag{5}$$

where i represents the imaginary unit, and p and j iterate from 0 to $m-1$. The absolute value of y denotes the amplitude of each frequency in the current deformed surface. Here, we normalize the amplitude of the decomposed wave frequencies by the amplitude of the dominant frequency for the surface deformation at current state. As shown in Fig. 3, the deformation configuration was categorized by FFT into different states, which are patternless, wrinkle, crease, fold, double, and ridge. (Note that the film and substrate are assumed to be perfectly bonded without delamination in the current study.) By performing FFT, we find the characteristics of the deformation states are quantitatively distinguishable in the frequency domain. The detailed FFT characterization of various patterns on curved structures in Fig. 3(*c*) is discussed as follows.

(i) *Patternless state*: Before the film–substrate system manifests instabilities on surface, the surface remains patternless under homogeneous deformation, and no wave frequency is detected by FFT.
(ii) *Wrinkling state*: When the critical strain for wrinkling is reached, the initially patternless film surface develops sinusoidal wave, and a single frequency is detected by FFT.
(iii) *Creasing state*. Unlike wrinkling, the creasing patterns are localized self-contacts developed on the initially patternless surface. The FFT spectrum of the creasing pattern consists of a wide range of wave frequencies with different amplitudes, as shown in Fig. 3(*c*) (crease).
(iv) *Folding state*: After the film wrinkles during surface deformation, the valley regions of the wrinkles may further form self-contacts, giving the folding state [41]. It has a dominant wrinkling frequency coupled with many low amplitude wave frequencies, which represent the wave components close to the tip of the fold.
(v) *Doubling state*: Doubling is another post-buckling transition from the wrinkling state [22]. During doubling evolution, initial wrinkles bifurcate into two branches, and the branching process results in two dominating frequencies for the doubled state. The large-amplitude (dominant) frequency represents the wrinkling instability, and the other

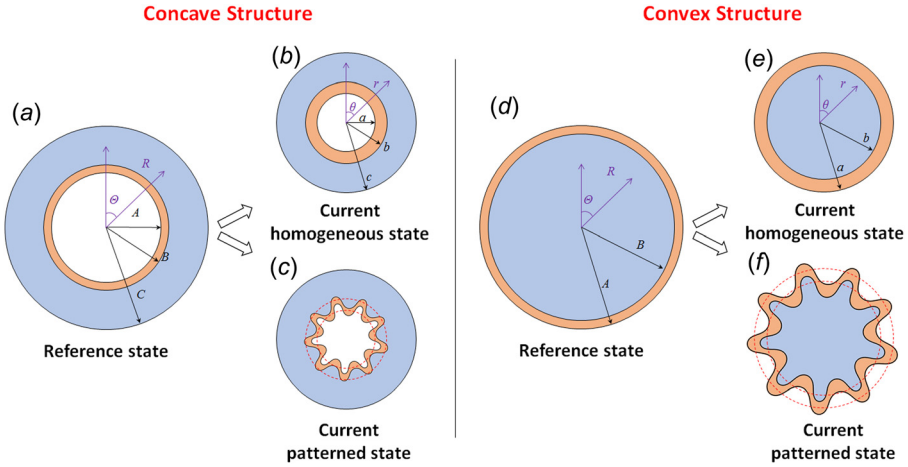

Fig. 2 Schematics for plane-strain deformation of concave film–substrate structure (*a*)–(*c*) and convex film–substrate structure (*d*)–(*f*). (*a*) and (*d*) represent the reference states; (*b*) and (*e*) denote the homogeneous current states; and (*c*) and (*f*) illustrate the patterned current states.

frequency with smaller amplitude represents the doubling instability, as shown in Fig. 3(*c*) (double).

(vi) *Ridging state*: Ridge is a height-limited regional localization that has a higher amplitude compared with wrinkle. For a curved film–substrate structure, it is usually difficult to distinguish ridge from wrinkle qualitatively. However, the wave frequency distribution of the FFT of ridge quantitatively shows that the ridging profile is not perfectly sinusoidal. There is a dominant wave frequency which corresponds to the wavelength of ridging, and this main frequency is accompanied by many small-amplitude wave components, as illustrated in Fig. 3(*c*) (ridge).

4 Theoretical Modeling for Wrinkling Instability on Curved Film–Substrate Structures

The surface stability of various film–substrate structures have been theoretically investigated with bifurcation and perturbation analysis, such as creasing on flat homogeneous half space [10], creasing and folding on half space with exponentially decayed modulus [37,73], wrinkling on flat film–substrate structure [13,16], instability bifurcations of thick-walled circular cylindrical [65,66,74–76], and buckling instability on cylindrical multilayer structure along circumferential and longitudinal directions [68,77]. In this paper, we will adopt the incremental theory to analyze the critical mismatch strain and critical wavenumber of wrinkling instabilities on curved film–substrate structures.

4.1 General Form of Governing Equations. Consider the plane-strain deformation of a tubular film–substrate structure, a material point at position $\mathbf{X}$ at the reference state moves to a new position $\mathbf{x}$ at the current state. The deformation gradient tensor is defined as

$$\mathbf{F} = \mathrm{Grad}\mathbf{x} = \frac{\partial \mathbf{x}}{\partial \mathbf{X}} \tag{6}$$

where the Jacobian of the deformation gradient $\det(\mathbf{F}) = 1$ for an incompressible material. The constitutive behavior of the incompressible hyperelastic material is defined through its strain energy density $W(\mathbf{F})$, and the nominal stress $\mathbf{S}$ and Cauchy stress $\boldsymbol{\sigma}$ are defined through

$$\mathbf{S} = \frac{\partial W}{\partial \mathbf{F}} - p\mathbf{F}^{-1} \tag{7}$$

$$\boldsymbol{\sigma} = \mathbf{F}\frac{\partial W}{\partial \mathbf{F}} - p\mathbf{I} \tag{8}$$

where p is the hydrostatic pressure to accomplish the incompressibility condition in the calculation.

The equilibrium equation in Lagrangian form satisfies

$$\mathrm{Div}\,\mathbf{S} = 0 \tag{9}$$

or in Eulerian form

$$\mathrm{div}\,\boldsymbol{\sigma} = 0 \tag{10}$$

4.2 Formulation Under Cylindrical Coordinates Under Homogeneous Deformation. To simplify the notations in the formulation, we use $\mathbf{e}_1, \mathbf{e}_2, \mathbf{e}_3$ to represent the unit vectors to the cylindrical coordinate r, θ, z at the current homogeneous state. Based on the incompressibility condition, the stretches in three principal axes along radial r, circumferential θ, and axial z directions are

$$\lambda_1 = \frac{\partial r}{\partial R} = \frac{1}{\lambda},\ \lambda_2 = \frac{r}{R} = \lambda,\ \lambda_3 = 1 \tag{11}$$

Along the principal axes, the principal Cauchy stress reads

$$\sigma_i = \lambda_i \frac{\partial W}{\partial \lambda_i} - p, i = 1, 2, 3 \tag{12}$$

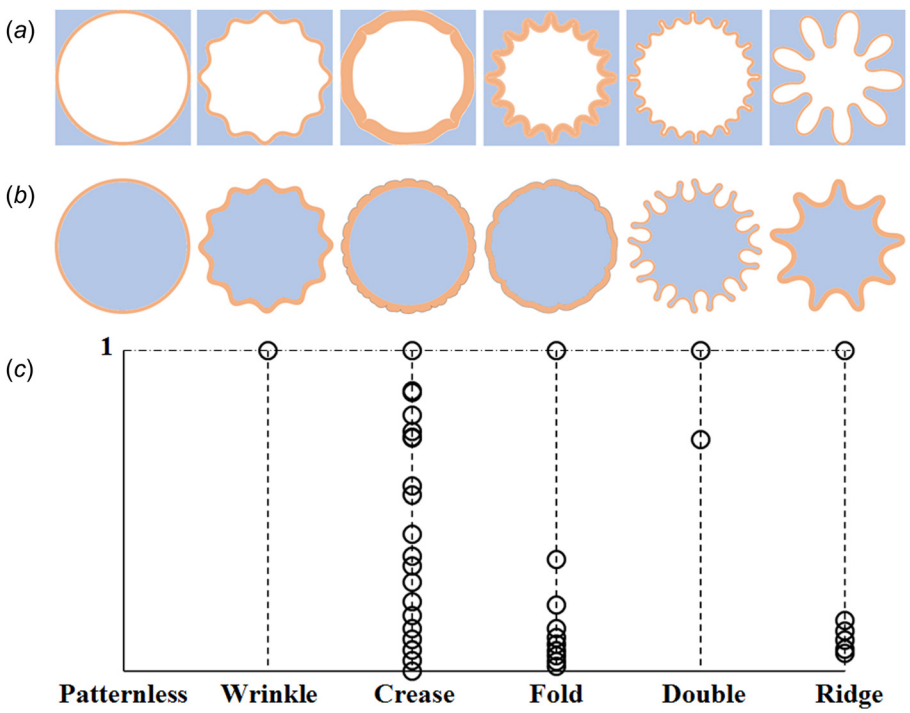

Fig. 3 Instability patterns on curved film–substrate structure and their FFT characterization. (*a*) and (*b*) Patternless state and instability patterns of wrinkle, crease, fold, double, and ridge on concave and convex film–substrate structures, respectively. (*c*) FFT characterization of the instability patterns.

The equilibrium condition at the current homogeneous state has the form

$$r\frac{d\sigma_1}{dr}+\sigma_1-\sigma_2=0 \tag{13}$$

The curved film–substrate structure should satisfy the traction-free boundary conditions on the surface of the film

$$\boldsymbol{\sigma}\mathbf{n}=0 \ \text{ at } \ r=a \tag{14}$$

and the continuity of displacement and traction at the film–substrate interface gives

$$\|\mathbf{u}\|=0, \|\boldsymbol{\sigma}\mathbf{n}\|=\mathbf{0} \ \text{ at } \ r=b \tag{15}$$

where $\mathbf{n}$ denotes the normal unit vector of the surface or interface at the current state, and $\|\|$ represents the jump of a quantity.

4.3 Incremental Equations. The incremental method for thick-walled tube instability was developed by Haughton and Ogden [78]. Consider $\mathbf{u}(\mathbf{x})=\dot{\mathbf{x}}(\mathbf{X})$ as the incremental displacement vector, and define the incremental deformation gradient $\dot{\mathbf{F}}_0$ as

$$\dot{\mathbf{F}}_0=\dot{\mathbf{F}}\mathbf{F}^{-1}=\operatorname{grad}\mathbf{u}=\begin{bmatrix} u_{r,r} & \frac{1}{r}(u_{r,\theta}-u_\theta) \\ u_{\theta,r} & \frac{1}{r}(u_{\theta,\theta}+u_r)\end{bmatrix} \tag{16}$$

with u_r, u_θ the incremental displacement in the radial and circumferential directions, respectively.

The incompressibility condition in the incremental form reads

$$\operatorname{tr}\dot{\mathbf{F}}_0=0 \tag{17}$$

which further gives

$$u_{r,r}+\frac{1}{r}(u_{\theta,\theta}+u_r)=0 \tag{18}$$

The incremental nominal stress is then derived as

$$\dot{\mathbf{S}}=D\dot{F}-\dot{p}\mathbf{F}^{-1}+p\mathbf{F}^{-1}\dot{\mathbf{F}}\mathbf{F}^{-1} \tag{19}$$

where $\mathbf{D}$ is the elasticity tensor

$$\mathbf{D}=\frac{\partial^2 W}{\partial\mathbf{F}\partial\mathbf{F}} \tag{20}$$

The corresponding form of the incremental nominal stress at the current state is defined through

$$\dot{\mathbf{S}}_0=\mathbf{B}\dot{\mathbf{F}}_0+p\dot{\mathbf{F}}_0-\dot{p}\mathbf{I} \tag{21}$$

where $\mathbf{B}$ represents the fourth-order tensor of instantaneous elastic moduli. Components of $\mathbf{B}$ are listed below [79]

$$B_{ijij}=B_{jjii}=\lambda_i\lambda_j W_{ij} \tag{22}$$

$$B_{ijij}=\frac{\lambda_i W_i-\lambda_j W_j}{\lambda_i^2-\lambda_j^2}\lambda_i^2,\ \lambda_i\neq\lambda_j \tag{23}$$

$$B_{ijji}=B_{jiij}=B_{ijij}-\lambda_i W_i,\ i\neq j \tag{24}$$

where $W_i=\partial W/\partial\lambda_i$ and $W_{ij}=\partial^2 W/\partial\lambda_i\lambda_j$ (no summation of index).

The equilibrium equation in terms of the incremental nominal stress at the current state satisfies

$$\operatorname{div}\dot{\mathbf{S}}_0=0 \tag{25}$$

Furthermore, the traction-free condition in the incremental form at the current state is

$$\dot{\mathbf{S}}^T{}_0\mathbf{n}=0 \tag{26}$$

5 Surface Instability Analysis and Discussions

The film–substrate system is modeled as neo-Hookean materials for both the film and substrate, whose strain energy function is defined as

$$W=\frac{\mu}{2}\left(\lambda_1^2+\lambda_2^2+\lambda_3^2-3\right) \tag{27}$$

where $\mu=\mu_f$ when $A<R<B$ for concave structures ($B<R<A$ for convex structures) and $\mu=\mu_s$ when $R>B$ for concave structures ($0<R<B$ for convex structures). Here, μ_f and μ_s are the initial shear moduli of the film and substrate, respectively.

From the strain energy function Eq. (27) and the incompressibility condition Eq. (18), we can derive the equilibrium equations in the incremental form as

$$\begin{aligned}&B_{1111}u_{r,rr}+\left(B_{1111,r}+p_{,r}+\frac{1}{r}B_{1111}\right)u_{r,r}+B_{2121}\frac{1}{r^2}u_{r,\theta\theta}\\&+\left(\frac{1}{r}B_{1122,r}-B_{2222}\frac{1}{r^2}\right)u_r+\left(\frac{1}{r}B_{2112}+B_{1122}\frac{1}{r}\right)u_{\theta,r\theta}\\&+\left(B_{1122,r}\frac{1}{r}-B_{2222}\frac{1}{r^2}-B_{2121}\frac{1}{r^2}\right)u_{\theta,\theta}-\dot{p}_{,r}=0\end{aligned} \tag{28}$$

$$\begin{aligned}&B_{1212}u_{\theta,rr}+B_{2222}\frac{1}{r^2}u_{\theta,\theta\theta}+\left(B_{1212,r}+\frac{1}{r}B_{1212}\right)u_{\theta,r}\\&-\left(B_{1221,r}\frac{1}{r}+B_{2121}\frac{1}{r^2}+p_{,r}\frac{1}{r}\right)u_\theta\\&+\left(B_{1221}\frac{1}{r}+\frac{1}{r}B_{2211}\right)u_{r,r\theta}+\left(B_{1221,r}\frac{1}{r}+B_{2222}\frac{1}{r^2}\right.\\&\left.+B_{2121}\frac{1}{r^2}+p_{,r}\frac{1}{r}\right)u_{r,\theta}-\frac{1}{r}\dot{p}_{,\theta}=0\end{aligned} \tag{29}$$

To solve for the critical mismatch strain and wavenumber of the instability problem, we assume the solutions have the form

$$\begin{aligned}u_r&=U_r(r)\cos(n\theta)\\u_\theta&=U_\theta(r)\sin(n\theta)\\\dot{p}&=P(r)\cos(n\theta)\end{aligned} \tag{30}$$

where n is the wrinkling wavenumber on the film surface.

From the incompressibility condition in Eq. (18), we can eliminate $U_\theta(r)$ and rewrite Eqs. (28) and (29) as

$$\begin{aligned}&\left(rB_{1122,r}-B_{2222}-n^2B_{2121}\right)U_r\\&+r^2\left(B_{1111,r}+p_{,r}+\frac{1}{r}B_{1111}\right)U_{r,r}+r^2B_{1111}U_{r,rr}\\&+n(rB_{1122,r}-B_{2222}-B_{2121})U_\theta\\&+rn(B_{2112}+B_{1122})U_{\theta,r}-r^2P_{,r}=0\end{aligned} \tag{31}$$

$$\begin{aligned}&n(rB_{1221,r}+B_{2222}+B_{2121}+rp_{,r})U_r+nr(B_{1221}+B_{2211})U_{r,r}\\&+\left(rB_{1221,r}+B_{2121}+n^2B_{2222}+rp_{,r}\right)U_\theta\\&-r^2\left(B_{1212,r}+\frac{1}{r}B_{1212}\right)U_{\theta,r}-r^2B_{1212}U_{\theta,rr}-rnP=0\end{aligned} \tag{32}$$

with the traction-free boundary conditions at $r=a$

$$\frac{1}{r}B_{1212}(u_{r,\theta}-u_\theta+ru_{\theta,r})=0 \tag{33}$$

$$\left(B_{1111}+\lambda_1\frac{\partial W}{\partial\lambda_1}-B_{1122}\right)u_{r,r}-\dot{p}=0 \tag{34}$$

the displacement condition for concave structure at $r=c$, and for convex structure at $r=0$

$$u_r=0,\ u_r'=0 \tag{35}$$

and the continuity condition for displacement and traction at $r=b$

$$\|u_r\|=0,\ \|u_r'\|=0 \tag{36}$$

$$\left\|\frac{1}{r}B_{1212}(u_{r,\theta}-u_\theta+ru_{\theta,r})\right\|=0 \tag{37}$$

$$\left\|\left(B_{1111}+\lambda_1\frac{\partial W}{\partial\lambda_1}-B_{1122}\right)u_{r,r}-\dot{p}\right\|=0 \tag{38}$$

where $\|\ \|$ denotes the jump of certain quantity at the interface as defined previously.

For neo-Hookean material, we have $B_{1122}=B_{2211}=B_{2112}=B_{1221}=0$. The only nonzero components of $\mathbf{B}$ are

$$B_{1111}=B_{1212}=\frac{\mu}{\lambda^2} \tag{39}$$

$$B_{2222}=B_{2121}=\mu\lambda^2 \tag{40}$$

where λ and $1/\lambda$ are the principal stretch along the circumferential θ and radial r directions, respectively, as defined in Eq. (11). We will specify $\lambda=\lambda_f$ for the film and $\lambda=\lambda_s$ for the substrate, when it is needed in later parts of the analysis.

From the equilibrium condition Eq. (13), we have

$$\frac{1}{\mu}p_{,r}=\frac{1}{r}\left(2-\lambda^2-\frac{1}{\lambda^2}\right) \tag{41}$$

By plugging Eq. (41) into Eqs. (31) and (32), we can eliminate p and write the final fourth-order ordinary differential equation (ODE) as

$$\begin{aligned}&U''''+\frac{1}{r}(4\lambda^2+2)U'''+\frac{1}{r^2}(8\lambda^2-n^2\lambda^4-3-n^2)U''\\&+\frac{n^2}{r^3}\left(2\lambda^6-3\lambda^4+\frac{3}{n^2}-\frac{4\lambda^2}{n^2}+1-2\lambda^2\right)U'\\&+\frac{n^2}{r^4}\left(3-\lambda^4-\frac{3}{n^2}+\frac{4\lambda^2}{n^2}+n^2\lambda^4-4\lambda^2\right)U=0\end{aligned} \tag{42}$$

The boundary conditions are rewritten in terms of (U, U', U'', U''') at film surface $r=a$

$$\frac{\mu}{\lambda^2}\left[r\frac{1}{n}U''+\frac{1}{n}U'+\frac{1}{r}\left(n-\frac{1}{n}\right)U\right]=0\quad\frac{2\mu}{\lambda^2}U'-P=0 \tag{43}$$

and at substrate $r=c$ for concave structure, or $r=0$ for convex structure

$$U=0,\ U'=0 \tag{44}$$

For the interface, we have the continuity condition for displacement and traction at $r=b$

$$\|U\|=0,\ \|U'\|=0 \tag{45}$$

$$\begin{aligned}&\left\|\frac{\mu}{\lambda^2}\left[r\frac{1}{n}U''+\frac{1}{n}U'+\frac{1}{r}\left(n-\frac{1}{n}\right)U\right]\right\|=0\\&\left\|\frac{2\mu}{\lambda^2}U'-P\right\|=0\end{aligned} \tag{46}$$

The fourth-order differential equation can be written in a matrix form

$$U''''-A_{44}U'''-A_{43}U''-A_{42}U'-A_{41}U=0 \tag{47}$$

$$\begin{aligned}&\mathbf{Y}'=\mathbf{AY}\\&\mathbf{A}(r)=\begin{bmatrix}0&1&0&0\\0&0&1&0\\0&0&0&1\\A_{41}&A_{42}&A_{43}&A_{44}\end{bmatrix}\\&\mathbf{Y}(r)=\begin{bmatrix}U&U'&U''&U'''\end{bmatrix}^{\mathrm{T}}\end{aligned} \tag{48}$$

with the coefficients

$$\begin{aligned}A_{41}&=-\frac{n^2}{r^4}\left(3-\lambda^4-\frac{3}{n^2}+\frac{4\lambda^2}{n^2}+n^2\lambda^4-4\lambda^2\right)\\A_{42}&=-\frac{n^2}{r^3}\left(2\lambda^6-3\lambda^4+\frac{3}{n^2}-\frac{4\lambda^2}{n^2}+1-2\lambda^2\right)\\A_{43}&=-\frac{1}{r^2}(8\lambda^2-n^2\lambda^4-3-n^2)\\A_{44}&=-\frac{1}{r}(4\lambda^2+2)\end{aligned} \tag{49}$$

Now let's assume the current state is the onset of the wrinkling. The corresponding homogeneous configuration of the substrate is stress free (i.e., the circumferential principal stretch of the substrate $\lambda_s=1$), and the corresponding homogeneous configuration of the film has circumferential principal stretch λ_f induced by the mismatch strain at the film–substrate interface. From the incompressible condition at the current homogeneous state, we can calculate

$$\lambda_f=\frac{r}{\sqrt{r^2-\left[(1-\varepsilon_M)^2-1\right]B^2}} \tag{50}$$

where B is the interfacial radius at the reference state, as illustrated in Fig. 2.

The fourth-order ODE in Eq. (47) is applicable to both the film and the substrate. There are in total eight boundary conditions to be considered when solving the problem: two traction-free conditions at the film surface (Eq. (43)), two displacement conditions at the far-end of the substrate ($r=c$ for concave structure and $r=0$ for convex structure) (Eq. (44)), and four continuity conditions for traction and displacement at the interface (Eq. (45)). To solve the system, we first integrate the ODE from both the film and the substrate sides to the interface by guessing two sets of solutions which satisfy the four boundary conditions in Eqs. (43) and (44) for the film and the substrate, respectively. We further match the four continuity boundary conditions (Eq. (45)) at the film–substrate interface. The explicit matrix form of Eq. (45) is shown in the Appendix. To have nontrivial solutions, the determinant of the interface condition matrix must vanish. We can then numerically solve the eigenvalue problem to search for the critical mismatch strain $\varepsilon_M^{\mathrm{Wrinkle}}$ for wrinkling of the curved film–substrate structure.

To explore the curvature effect on wrinkling, we examine critical mismatch strain $\varepsilon_M^{\mathrm{Wrinkle}}$ and critical wavenumber n_c for the film–substrate system with different normalized curvatures $\rho=-0.1,-0.04,-0.02,\ 0,\ 0.02, 0.04$, and 0.1, as shown in Fig. 4(*a*). We plot critical mismatch strain for film–substrate

system with modulus ratio μ_f/μ_s ranging from 10 to 10^4 in Fig. 4(*a*). The solid curves from left to right denote the critical mismatch strains for wrinkling of the film-substrate system with normalized curvature $\rho = 0$, 0.02, 0.04, and 0.1, respectively [15,37,41]. The dotted curves from left to right are for structures with the normalized curvature $\rho = -0.02$, -0.04, and -0.1, respectively. From Fig. 4(*a*), we can see that for different normalized curvature amplitudes, the critical mismatch strains for wrinkling deviate significantly when the modulus ratio is beyond 100. Under this condition, the curvature of film–substrate structure delays wrinkling compared with the flat film–substrate structure. In addition, Fig. 4(*b*) shows the critical wavenumber for the three examined normalized curvature amplitudes. Our calculation shows that the critical wavenumber for wrinkling is the same for concave and convex structures with the same curvature magnitudes.

6 Phase Diagrams for Multimodal Surface Instabilities on Curved Film–Substrate Systems

Wrinkling is a mode of surface instability that occurs under relatively low mismatch strains and can be predicted analytically as discussed in Sec. 5. As the mismatch strain further increases, advanced modes of surface instabilities such as creasing, folding, doubling, and ridging may occur. To quantitatively understand and predict various modes of surface instabilities in curved film–substrate structures, we adopt the finite element method to systematically investigate the occurrence and evolution of multimodal surface instabilities and, in particular, the curvature's effects on these instabilities.

We implement the two-dimensional plane-strain tubular film–substrate structures with negative and positive curvatures illustrated in Figs. 2(*a*) and 2(*d*) into finite element models using software package ABAQUS/STANDARD. The 2D plane-strain four-node bilinear element with reduced integration and hourglass control (CPE4RH) is used for the negative-curvature case. For the positive-curvature case, in order to satisfy the incompressibility requirement, the 3D eight-node linear brick with reduced integration, hourglass control, and hybrid with constant pressure (C3D8RH) is used. We validate the mesh insensitivity of the models using different mesh densities, which give surface deformation with the same critical mismatch strain and instability patterns. A random perturbation with small amplitude is applied to the mesh of film surface to trigger the instability during loading. We also validate that the instability patterns are perturbation insensitive. A self-contact interaction with the type of frictionless and "hard contact" is applied to the film surface to avoid element penetration during creasing and folding deformations.

The incompressible neo-Hookean constitutive model is adopted for both the film and substrate with different shear modulus μ_f and μ_s, respectively. The modulus ratio μ_f/μ_s ranges from 10^{-1} to 10^4 in our simulation. The mismatch strain ε_M can be induced by prestretching the substrate, shrinking the substrate, or expanding the film. The path independency of the loading method has been discussed in literature [40]. To induce the film–substrate mismatch strain in our simulation, for the negative-curvature system, we prestretch the substrate along the radial direction, bond the film on the substrate, and then relax the prestretch in the substrate. For the positive-curvature system, we directly shrink the substrate (without prestretch) by assigning thermal expansion coefficient to the substrate and applying thermal loading to control the shrinkage. The instability patterns are evaluated and categorized by the FFT method introduced in Sec. 3. In the simulation, creasing is usually hard to be triggered on smooth surface without sufficient imperfection or undulation. Following previous studies, the creasing instability is predicted to occur, when the compressive strain on the film surface reaches a critical value, 0.35 [17,46].

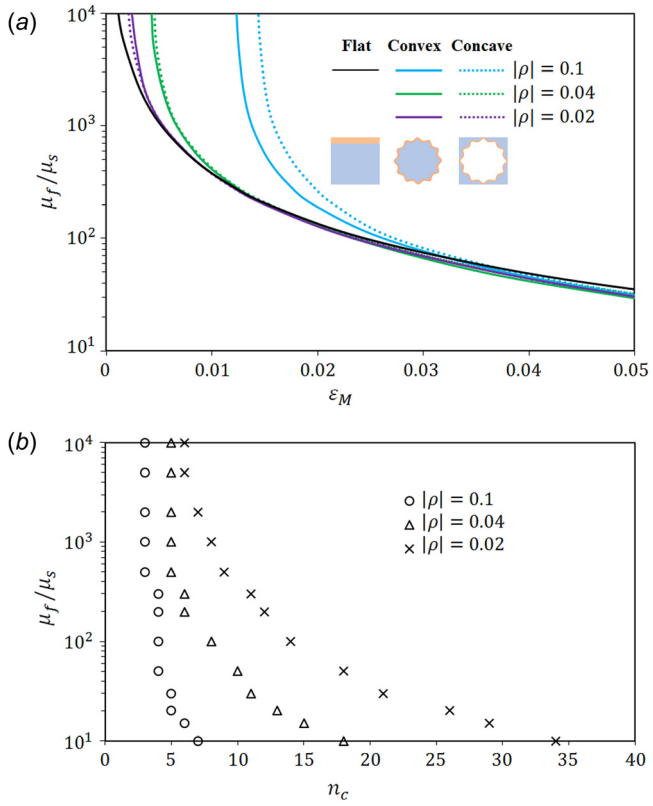

Fig. 4 Curvature effects on the onset of wrinkling for the curved film–substrate systems. (*a*) Critical mismatch strain for systems with different normalized curvatures. The solid curves from left to right are for $\rho = 0$, 0.02, 0.04, and 0.1. The dotted curves from left to right are for $\rho = -0.02$, -0.04, and -0.1 (color version online). (*b*) Changing of critical mode number n_c with film–substrate modulus ratio for structures with different curvatures.

We summarize the results from the finite element simulations in phase diagrams given in Figs. 5(*a*)–5(*e*), for five normalized curvatures $\rho = -0.1, -0.04,\ 0,\ 0.04,$ and 0.1, respectively. Each phase on the phase diagrams represents a type of surface instability pattern as categorized by the FFT method introduced in Sec. 3, and the governing parameters for phase diagrams are normalized curvature, modulus ratio, and mismatch strain of the film–substrate system. From Fig. 5, it can be seen that the phase diagrams of surface instability patterns share a number of common features. Patternless and wrinkling phases occur at relatively small mismatch strains. Compared with patternless and wrinkling, other modes of instabilities take place when the mismatch strains are relatively large. Creasing and folding states develop in film–substrate structures with relatively low modulus ratios, while doubling and ridging states require higher modulus ratios. Despite these common features, the curvatures of film–substrate structures can affect the instability patterns significantly (Fig. 5). To understand the film–substrate curvature's effects, we compare the surface instability patterns in film–substrate structures with different curvatures but the same mismatch strains and modulus ratios, as demonstrated in Figs. 5(*a*)–5(*e*).

Creasing is promoted by negative curvature and suppressed by positive curvature. The region of creasing instability is marked by orange color in the phase diagrams in Fig. 5. It has been proven that for film–substrate system with relatively small modulus ratio $\mu_f/\mu_s < 1.3$, the patternless-creasing transition takes place when

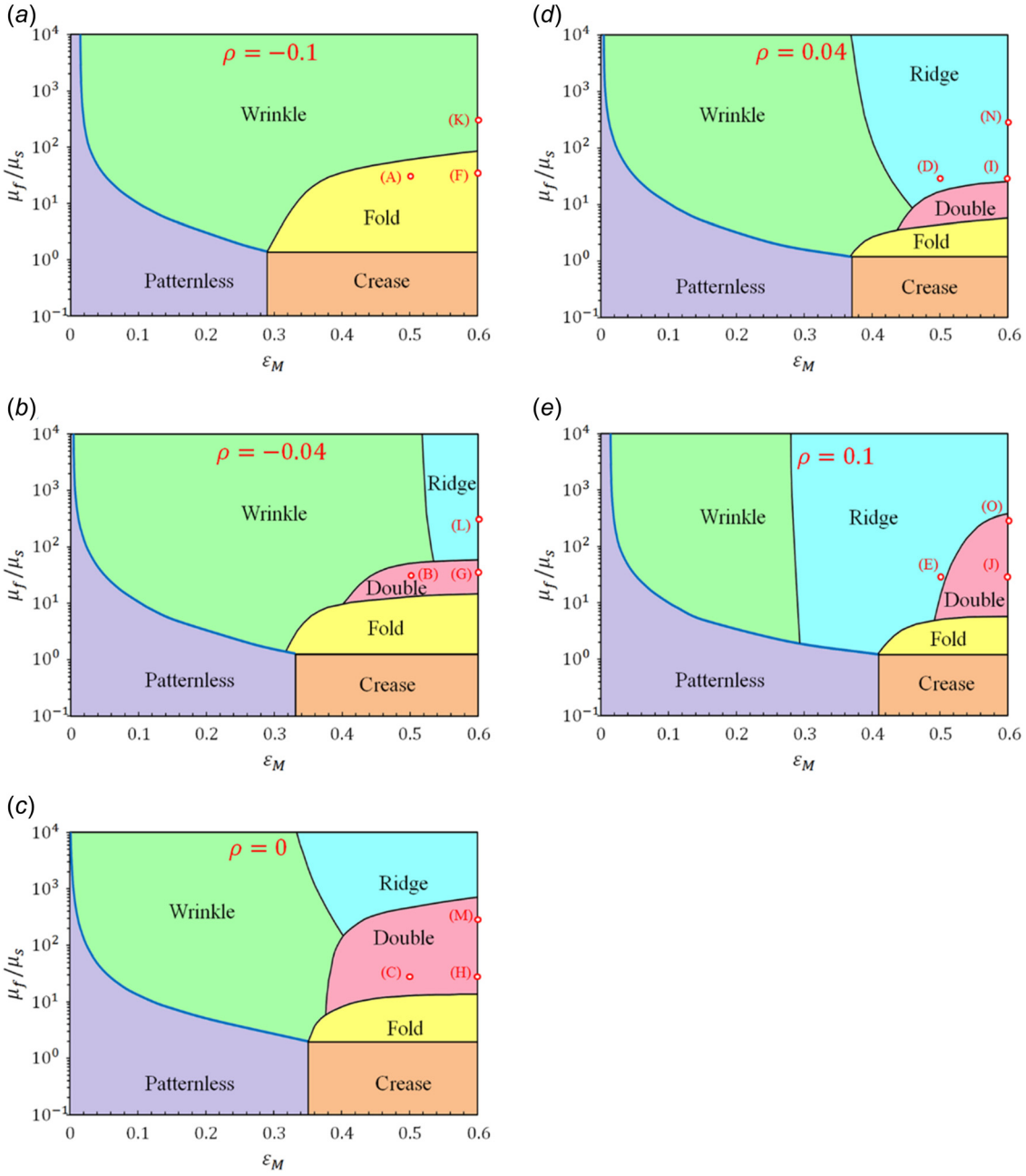

Fig. 5 Phase diagrams for mismatch-strain induced instability patterns on curved film–substrate structure with different normalized curvatures. (*a*)$\rho = -0.1$, (*b*)$\rho = -0.04$, (*c*)$\rho = 0$, (*d*)$\rho = 0.04$, and (*e*)$\rho = 0.1$. Blue solid curve denotes the theoretical buckling condition. Black solid curves represent simulated phase boundaries. Colored regions represent different phases: purple for flat, green for winkle, orange for crease, yellow for fold, red for double, blue for ridge, and dark blue for disordering. The instability morphologies of the highlighted points (A–O) are shown in Fig. 6 (see color figure online).

the compressive strain on the film surface exceeds 0.35 [17,40,46]. Before this critical point, the system maintains homogeneous deformation as illustrated in Figs. 2(*b*) and 2(*e*). As explained in Sec. 2, for curved film–substrate structure with mismatch strain, the circumferential compressive strain distribution along the thickness of the film is not uniform. Considering the current homogeneous state of the curved film–substrate structure as the critical state for creasing (i.e., the compressive strain at the film surface $R = A$ is 0.35), we can solve for the corresponding critical mismatch strain for creasing $\varepsilon_M^{\text{Crease}}$ from Eq. (4)

$$\varepsilon_M^{\text{Crease}}(\rho) = 1 - \frac{-231\rho + 20\sqrt{231\rho^2 + 169}}{231\rho^2 + 400} \tag{51}$$

The critical mismatch strain for the selected cases $\rho = -0.1$, -0.04, 0, 0.04, and 0.1 is then calculated to be $\varepsilon_M^{\text{Crease}} = 0.29, 0.33, 0.35, 0.38,$ and 0.41, respectively. Additionally, for normalized curvatures in the range of $-0.5 \le \rho \le 0.5$, the $\varepsilon_M^{\text{Crease}}$ can be approximated by the following linear function of ρ:

$$\varepsilon_M^{\text{Crease}}(\rho) = 0.53\rho + 0.35, -0.5 \le \rho \le 0.5 \tag{52}$$

Evidently, the critical mismatch strain for creasing increases with the normalized curvature of the film–substrate structure. For curved film–substrate structure with $\rho < 0$, the critical mismatch strain $\varepsilon_M^{\text{Crease}}$ for creasing is smaller than 0.35. On the contrary, $\varepsilon_M^{\text{Crease}}$ is larger than 0.35 for system with $\rho > 0$.

Folding is promoted by negative curvature and suppressed by positive curvature. The curvature of the film–substrate structure has significant effects on the phase boundaries between folding and adjacent phases including wrinkling, doubling, and ridging. From Figs. 5(*a*)–5(*e*), it reveals that the area of the folding region (marked by yellow) on the phase diagram decreases significantly when the surface of the film–substrate structure goes from concave to flat, then to convex (ρ goes from negative to zero, then to positive), which means that folding is promoted by concave surface. Folding can take place right after wrinkling instability when the modulus ratio is relatively low (near $\mu_f/\mu_s = 1.3$). In this case, the local film strain at the wrinkling valley reaches the critical mismatch strain for creasing ($\varepsilon_f = 0.35$) immediately after wrinkling, and the surface initiates a crease tip at the valley of the wrinkle. Folding can also manifest upon well-developed wrinkles, when μ_f/μ_s is larger. The phase diagram in Fig. 5(*a*) for concave structure $\rho = -0.1$ shows that the critical mismatch strain to trigger folding is within a range of $0.29 \le \varepsilon_M \le 0.40$, for modulus ratio $1.3 \le \mu_f/\mu_s \le 80$. For concave surface with normalized curvature $\rho = -0.04$ as shown in Fig. 5(*b*), folding initiates on film surface under mismatch strain $0.33 \le \varepsilon_M \le 0.35$, for modulus ratio $1.3 \le \mu_f/\mu_s \le 15$. Figure 5(*c*) illustrates the phase transitions for flat film–substrate structure ($\rho = 0$). From the phase diagram, we can see that the folding transition on film surface starts with mismatch strain $0.35 \le \varepsilon_M \le 0.45$, for modulus ratio $1.3 \le \mu_f/\mu_s \le 12$. For convex film–substrate structures, the folding region is even more significantly reduced, as shown in the phase diagrams in Figs. 5(*d*) and 5(*e*). The critical mismatch strain for folding is postponed to $0.37 \le \varepsilon_M \le 0.40$ and $0.41 \le \varepsilon_M \le 0.45$, for normalized film–substrate curvatures $\rho = 0.04$ and 0.1, respectively. Moreover, the range of modulus ratio for folding is shrunken to $1.3 \le \mu_f/\mu_s \le 6$ for both cases.

In general, negative curvature promotes folding by requiring relatively small mismatch strains for patternless-folding transition, and allowing relatively wide ranges of film–substrate modulus ratio for the folding phase. This trend can be understood as follows. The inhomogeneous distribution of the circumferential compressive strain throughout the thickness of the film leads to the curvature effect on surface instabilities. With the same interfacial mismatch strain ε_M between the film and substrate, concave structure gives higher compressive strain on the film surface than flat structure, and thus promotes folding. On the contrary, convex structure gives lower compressive strain on the film surface compared to the flat structure, and thus suppresses folding.

We further use a few points with the same modulus ratio and mismatch strain (i.e., $\mu_f/\mu_s = 30, \varepsilon_M = 0.5$ for points (A–E) and $\mu_f/\mu_s = 30, \varepsilon_M = 0.6$ for points (F–J)) on the phase diagrams with different normalized curvature (i.e., $\rho = -0.1, -0.04$, 0, 0.04, and 0.1) to discuss curvature's effect on folding, as shown in Figs. 6(*a*) and 6(*b*). Points (A) and (F) show folding instability on the film surface, for normalized film–substrate curvature $\rho = -0.1$. Folding disappears on film surface when the normalized film–substrate curvature is increased to $\rho = -0.04$ or larger. In these cases, other instability phases such as doubling and ridging are observed and will be discussed in the following parts.

Ridging is promoted by positive curvature and suppressed by negative curvature. On flat film–substrate structure, ridging instability is observed on film surface as an outward localization for systems with relatively high mismatch strains and modulus ratio. As discussed in Sec. 3, ridging is characterized by FFT and its wave frequency components reveal the nonaxisymmetric geometry compared with wrinkling. Its FFT spectrum shows a dominant wave frequency, which is accompanied by massive small-amplitude frequencies as shown in Fig. 3(*c*). Here, our simulation results further show that for curved film–substrate structures, the curvature plays an important role in determining the ridging phase.

The phase diagram in Fig. 5 indicates that the area of ridging zone increases with the normalized film–substrate curvature. Flat film–substrate structure ($\rho = 0$) shows that the range of the critical mismatch strain for wrinkling–ridging transition is within $0.30 \le \varepsilon_M \le 0.40$, for modulus ratio $\mu_f/\mu_s \ge 150$. For convex system with film–substrate curvature $\rho = 0.04$ shown in Fig. 5(*d*), the critical mismatch strain for ridging is in the region of $0.35 \le \varepsilon_M \le 0.45$, for a wide range of modulus ratio $\mu_f/\mu_s \ge 10$. By further increasing the normalized film–substrate curvature to $\rho = 0.1$, ridging can be triggered at a small mismatch strain around $\varepsilon_M = 0.30$ for very small modulus ratio $\mu_f/\mu_s \ge 1.3$ (illustrated in Fig. 5(*e*)). Ridge-folds or ridge-doubles will develop on film surface under continuous loading. On the contrary, for concave film–substrate structure ($\rho < 0$), ridging is significantly suppressed. As illustrated in Fig. 5(*b*) for system with normalized curvature $\rho = -0.04$, the triggering strain for ridging is postponed to $\varepsilon_M = 0.50$ compared with flat and convex film–substrate structure, and the corresponding range of modulus ratio for ridging is $\mu_f/\mu_s \ge 60$. If we further increase the normalized curvature of the system to $\rho = -0.1$, no ridging transition is observed on film surface, as shown in Fig. 5(*a*).

The contour plots for selected cases (A–E), (F–J), and (K–O) in Figs. 6(*a*)–6(*c*) illustrate how positive curvature (convex structure) promotes ridging and suppresses folding. For system with mismatch strains and modulus ratios $\varepsilon_M = 0.5, \mu_f/\mu_s = 30$, points (D) and (E) in column (*a*) show ridging instability for normalized film–substrate curvature $\rho = 0.04$ and 0.1, respectively. In column (*b*) with $\varepsilon_M = 0.6, \mu_f/\mu_s = 30$, ridge is observed for point (I) and ridge-double is seen for point (J). For system with $\varepsilon_M = 0.6, \mu_f/\mu_s = 300$ as shown in column (*c*), points (L) and (N) reveal ridging instability and point (O) develops ridge-double on film surface.

7 Conclusion

In this paper, we studied the curvature's effects on multimodal surface instabilities in tubular film–substrate structures, which are commonly found in nature and engineering applications. We proved that the curvature along with the mismatch strain and modulus ratio of the film–substrate system determines the occurrence of various instabilities including wrinkling, creasing, folding, doubling, and ridging. We applied the FFT method to characterize the surface instabilities quantitatively, by decomposing the wave frequencies of each instability mode. We then

provided a systematic study on the formation of multimodal surface instabilities on curved film–substrate structures with different curvatures through combined theoretical analysis and numerical simulation. We used the incremental theory to predict the critical mismatch strain for wrinkling and wavenumber for systems with different normalized film–substrate curvatures, under a wide range of film–substrate modulus ratio ($1 < \mu_f/\mu_s \leq 10^4$). The results showed that large curvature magnitudes can delay wrinkling significantly when the modulus ratio is larger than 100. Our finite element simulations on post-buckling of the curved film–substrate system showed that curvature plays an important role in determining the phase boundaries for various modes of instabilities. Concave structure (negative curvature) has the trend of promoting folding and suppressing ridging. Convex structure (positive curvature) promotes ridging and suppresses folding. A set of phase diagrams are calculated to systematically understand the curvature's effect on multimodal instabilities in film–substrate structures.

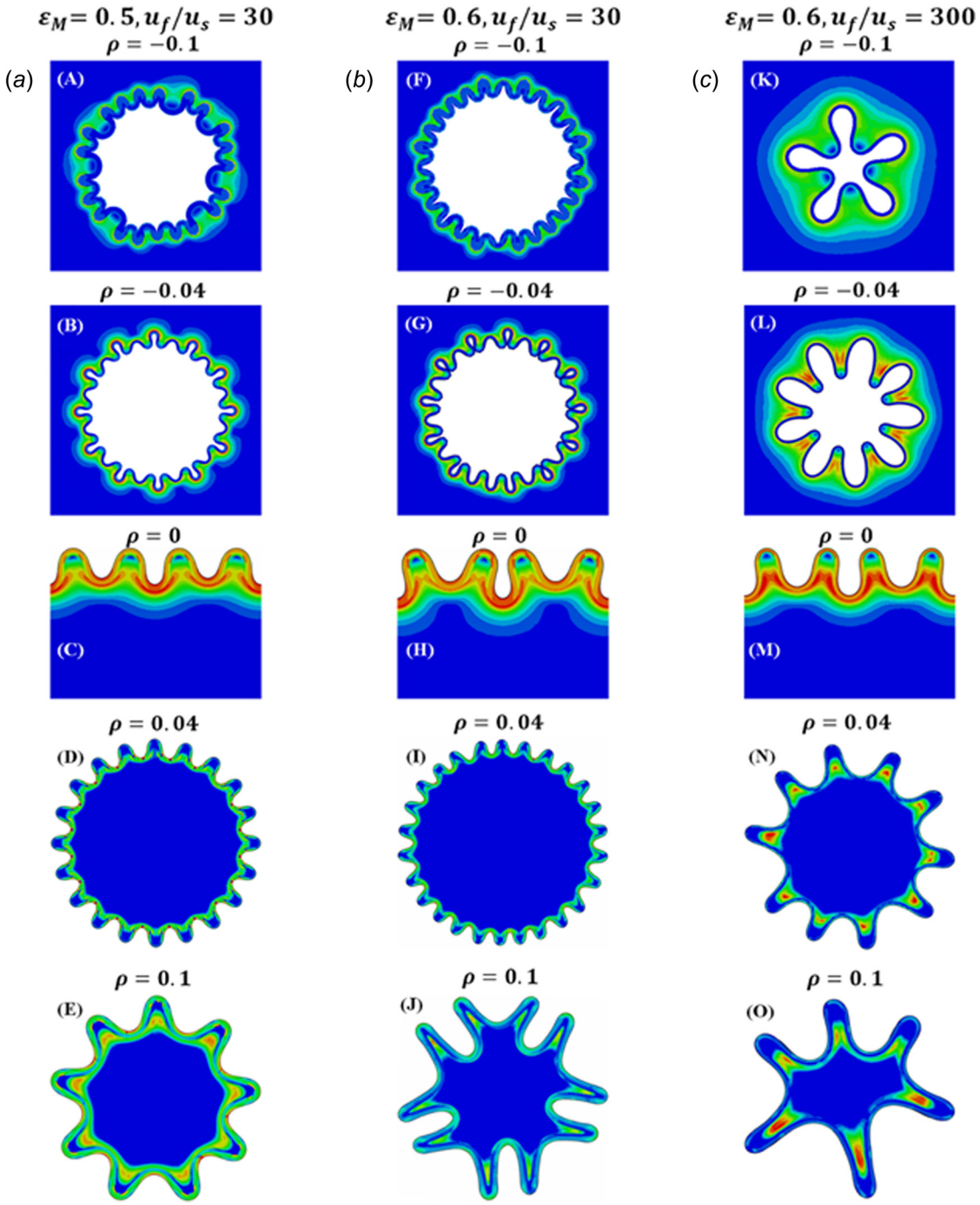

Fig. 6 The instability morphologies of the highlighted points (A–O) on the phase diagrams in Fig. 5. The contour plots show the maximum in-plane nominal strain for each case. The five rows from top to bottom in each column represent five different curvatures $\rho = -0.1, -0.04, 0, 0.04$, and 0.1. Column (*a*) includes (A–E), which have the mismatch strain and modulus ratio $\varepsilon_M = 0.5, \mu_f/\mu_s = 30$. Column (*b*) includes (F–J), which have the mismatch strain and modulus ratio $\varepsilon_M = 0.6, \mu_f/\mu_s = 30$. Column (*b*) includes (K–O), which have the mismatch strain and modulus ratio $\varepsilon_M = 0.6, \mu_f/\mu_s = 300$.

Acknowledgment

This work was supported by ONR (No. N00014-14-1-0528), MIT Institute for Soldier Nanotechnologies, and NSF (No. CMMI-1253495).

Appendix

The detail of derivation in Sec. 5 is partially shown here. The explicit form of Eq. (25) can be written as

$$\begin{aligned}
\dot{S}_{0rr,r} &= B_{1111,r}u_{r,r} + B_{1111}u_{r,rr} + B_{1122,r}\frac{1}{r}(u_{\theta,\theta}+u_r) - B_{1122}\frac{1}{r^2}(u_{\theta,\theta}+u_r) + B_{1122}\frac{1}{r}(u_{\theta,\theta r}+u_{r,r}) \\
&\quad + p_{,r}u_{r,r} + pu_{r,rr} - \dot{p}_{,r} \\
\dot{S}_{0\theta r,\theta} &= B_{2121,\theta}\frac{1}{r}(u_{r,\theta}-u_\theta) + B_{2121}\frac{1}{r}(u_{r,\theta\theta}-u_{\theta,\theta}) + B_{2112,\theta}u_{\theta,r} + B_{2112}u_{\theta,r\theta} + p_{,\theta}u_{\theta,r} + pu_{\theta,r\theta} \\
\dot{S}_{0r\theta,r} &= B_{1212,r}u_{\theta,r} + B_{1212}u_{\theta,rr} + B_{1221,r}\frac{1}{r}(u_{r,\theta}-u_\theta) - B_{1221}\frac{1}{r^2}(u_{r,\theta}-u_\theta) + B_{1221}\frac{1}{r}(u_{r,\theta r}-u_{\theta,r}) \\
&\quad + p_{,r}\frac{1}{r}(u_{r,\theta}-u_\theta) - p\frac{1}{r^2}(u_{r,\theta}-u_\theta) + p\frac{1}{r}(u_{r,\theta r}-u_{\theta,r}) \\
\dot{S}_{0\theta\theta,\theta} &= B_{2211,\theta}u_{r,r} + B_{2211}u_{r,r\theta} + B_{2222}\frac{1}{r}(u_{\theta,\theta\theta}+u_{r,\theta}) + B_{2222,\theta}\frac{1}{r}(u_{\theta,\theta}+u_r) + p\frac{1}{r}(u_{\theta,\theta\theta}+u_{r,\theta}) \\
&\quad + p_{,\theta}\frac{1}{r}(u_{\theta,\theta}+u_r) - \dot{p}_{,\theta}
\end{aligned} \tag{A2}$$

The boundary conditions in Eqs. (43)–(46) in matrix forms are shown here. First consider the traction-free condition at $r=a$

$$\mathbf{E}\mathbf{Y}_f(a) = 0$$

$$\mathbf{E} = \begin{bmatrix} \frac{1}{a}\left(2-\frac{1}{\lambda_f^2}-\frac{2}{n^2}+\frac{1}{n^2\lambda_f^2}\right) & -\frac{1}{n^2}\left(n^2\lambda_f^2-2+\frac{1}{\lambda_f^2}+\frac{2n^2}{\lambda_f^2}\right) & \frac{a}{n^2}\left(2+\frac{2}{\lambda_f^2}\right) & \frac{r^2}{n^2}\frac{1}{\lambda_f^2} \\ \frac{1}{a}\left(n-\frac{1}{n}\right) & \frac{1}{n} & a\frac{1}{n} & 0 \end{bmatrix} \tag{A3}$$

the displacement boundary condition at $r=c$

$$\mathbf{F}\mathbf{Y}_s(c) = 0 \quad \mathbf{F} = \begin{bmatrix} 1 & 0 & 0 & 0 \\ 0 & 1 & 0 & 0 \end{bmatrix} \tag{A4}$$

the traction continuity boundary condition at interface $r=b$

$$\begin{aligned}
&\mu_f\left[\frac{1}{b}\left(2-\frac{1}{\lambda_f^2}-\frac{2}{n^2}+\frac{1}{n^2\lambda_f^2}\right)U_f - \frac{1}{n^2}\left(n^2\lambda_f^2-2+\frac{1}{\lambda_f^2}+\frac{2n^2}{\lambda_f^2}\right)U_f' + \frac{b}{n^2}\left(2+\frac{2}{\lambda_f^2}\right)U_f'' + \frac{b^2}{n^2}\frac{1}{\lambda_f^2}U_f'''\right] \\
&= \mu_s\left[\frac{1}{b}\left(2-\frac{1}{\lambda_s^2}-\frac{2}{n^2}+\frac{1}{n^2\lambda_s^2}\right)U_s - \frac{1}{n^2}\left(n^2\lambda_s^2-2+\frac{1}{\lambda_s^2}+\frac{2n^2}{\lambda_s^2}\right)U_s' + \frac{b}{n^2}\left(2+\frac{2}{\lambda_s^2}\right)U_s'' + \frac{b^2}{n^2}\frac{1}{\lambda_s^2}U_s'''\right] \\
&\frac{\mu_f}{\lambda_f^2}\left[b\frac{1}{n}U_f'' + \frac{1}{n}U_f' + \frac{1}{b}\left(n-\frac{1}{n}\right)U_f\right] = \frac{\mu_s}{\lambda_s^2}\left[b\frac{1}{n}U_s'' + \frac{1}{n}U_s' + \frac{1}{b}\left(n-\frac{1}{n}\right)U_s\right]
\end{aligned} \tag{A5}$$

The matrix form of the boundary conditions at interface is

$$\mathbf{Q}\mathbf{Y}_f(b) = \mathbf{V}\mathbf{Y}_s(b)$$

where $\mathbf{Q}$ and $\mathbf{V}$ are coefficient matrixes for film and substrate, respectively,

$$\mathbf{Q} = \begin{bmatrix} Q11 & Q12 & Q13 & Q14 \\ Q21 & Q22 & Q23 & Q24 \end{bmatrix}$$
$$\mathbf{V} = \begin{bmatrix} V11 & V12 & V13 & V14 \\ V21 & V22 & V23 & V24 \end{bmatrix} \tag{A6}$$

$$Q11 = \frac{\mu_f}{b}\left(2 - \frac{1}{\lambda_f^2} - \frac{2}{n^2} + \frac{1}{n^2\lambda_f^2}\right)$$
$$Q12 = -\frac{\mu_f}{n^2}\left(n^2\lambda_f^2 - 2 + \frac{1}{\lambda_f^2} + \frac{2n^2}{\lambda_f^2}\right)$$
$$Q13 = \frac{\mu_f b}{n^2}\left(2 + \frac{2}{\lambda_f^2}\right)$$
$$Q14 = \mu_f \frac{b^2}{n^2}\frac{1}{\lambda_f^2} \tag{A7}$$
$$Q21 = \frac{\mu_f}{\lambda_f^2}\frac{1}{b}\left(n - \frac{1}{n}\right)$$
$$Q22 = \frac{\mu_f}{\lambda_f^2}\frac{1}{n}$$
$$Q23 = \frac{\mu_f}{\lambda_f^2}\frac{b}{n}$$
$$Q24 = 0$$

$$V11 = \frac{\mu_s}{b}\left(2 - \frac{1}{\lambda_s^2} - \frac{2}{n^2} + \frac{1}{n^2\lambda_s^2}\right)$$
$$V12 = -\frac{\mu_s}{n^2}\left(n^2\lambda_s^2 - 2 + \frac{3}{\lambda_s^2}\right)$$
$$V13 = \frac{\mu_s b}{n^2}\left(2 + \frac{2}{\lambda_s^2}\right)$$
$$V14 = \mu_s \frac{b^2}{n^2}\frac{1}{\lambda_s^2}$$
$$V21 = \frac{\mu_s}{\lambda_s^2}\frac{1}{b}\left(n - \frac{1}{n}\right)$$
$$V22 = \frac{\mu_s}{\lambda_s^2}\frac{1}{n}$$
$$V23 = \frac{\mu_s}{\lambda_s^2}\frac{b}{n}$$
$$V24 = 0$$

Then, we write the displacement continuity boundary condition at interface $r = b$

$$U_s - U_f = 0$$
$$U'_s - U'_f = 0 \tag{A8}$$

The matrix form of Eq. (A8) is

$$\mathbf{TY}_f(b) = \mathbf{TY}_s(b)$$
$$\mathbf{T} = \begin{bmatrix} 1 & 0 & 0 & 0 \\ 0 & 1 & 0 & 0 \end{bmatrix} \tag{A9}$$

The eigenvalue problem in Eqs. (A6)–(A9) can then be solved numerically to search for the critical film–substrate mismatch strain for wrinkling.

References

[1] Cao, Y.-P., Li, B., and Feng, X.-Q., 2012, "Surface Wrinkling and Folding of Core–Shell Soft Cylinders," Soft Matter, **8**(2), pp. 556–562.
[2] Tallinen, T., Biggins, J. S., and Mahadevan, L., 2013, "Surface Sulci in Squeezed Soft Solids," Phys. Rev. Lett., **110**(2), p. 024302.
[3] Rogers, J. A., Someya, T., and Huang, Y., 2010, "Materials and Mechanics for Stretchable Electronics," Science, **327**(5973), pp. 1603–1607.
[4] Fu, H., Xu, S., Xu, R., Jiang, J., Zhang, Y., Rogers, J. A., and Huang, Y., 2015, "Lateral Buckling and Mechanical Stretchability of Fractal Interconnects Partially Bonded Onto an Elastomeric Substrate," Appl. Phys. Lett., **106**(9), p. 091902.
[5] Zhang, Y., Huang, Y., and Rogers, J. A., 2015, "Mechanics of Stretchable Batteries and Supercapacitors," Curr. Opin. Solid State Mater. Sci., **19**(3), pp. 190–199.
[6] Wang, W., Yao, L., Cheng, C.-Y., Zhang, T., Atsumi, H., Wang, L., Wang, G., Anilionyte, O., Steiner, H., and Ou, J., 2017, "Harnessing the Hygroscopic and Biofluorescent Behaviors of Genetically Tractable Microbial Cells to Design Biohybrid Wearables," Sci. Adv., **3**(5), p. e1601984.
[7] Zhang, Z., Zhang, T., Zhang, Y. W., Kim, K.-S., and Gao, H., 2012, "Strain-Controlled Switching of Hierarchically Wrinkled Surfaces Between Superhydrophobicity and Superhydrophilicity," Langmuir, **28**(5), pp. 2753–2760.
[8] Cao, C., Feng, Y., Zang, J., López, G. P., and Zhao, X., 2015, "Tunable Lotus-Leaf and Rose-Petal Effects Via Graphene Paper Origami," Extreme Mech. Lett., **4**, pp. 18–25.
[9] Cao, G., Chen, X., Li, C., Ji, A., and Cao, Z., 2008, "Self-Assembled Triangular and Labyrinth Buckling Patterns of Thin Films on Spherical Substrates," Phys. Rev. Lett., **100**(3), p. 036102.
[10] Biot, M., 1963, "Surface Instability of Rubber in Compression," Appl. Sci. Res., Sect. A, **12**(2), pp. 168–182.
[11] Hutchinson, J. W., 2013, "The Role of Nonlinear Substrate Elasticity in the Wrinkling of Thin Films," Philos. Trans. A: Math., Phys. Eng. Sci., **371**(1993), p. 20120422.
[12] Shield, T., Kim, K., and Shield, R., 1994, "The Buckling of an Elastic Layer Bonded to an Elastic Substrate in Plane Strain," ASME J. Appl. Mech., **61**(2), pp. 231–235.
[13] Sun, J.-Y., Xia, S., Moon, M.-W., Oh, K. H., and Kim, K.-S., 2011, "Folding Wrinkles of a Thin Stiff Layer on a Soft Substrate," Proc. R. Soc. A: Math., Phys. Eng. Sci., **468**(2140), pp. 932–953.
[14] Allen, H., 1969, *Analysis and Design of Structural Sandwich Panels*, B. G. Neal, ed., Pergamon Press, Elmsford, NY.
[15] Cao, Y., and Hutchinson, J. W., 2012, "Wrinkling Phenomena in Neo-Hookean Film/Substrate Bilayers," ASME J. Appl. Mech., **79**(3), p. 031019.
[16] Cao, Y., and Hutchinson, J. W., 2011, "From Wrinkles to Creases in Elastomers: The Instability and Imperfection-Sensitivity of Wrinkling," Proc. R. Soc. A: Math., Phys. Eng. Sci., **468**(2137), pp. 94–115.
[17] Hong, W., Zhao, X., and Suo, Z., 2009, "Formation of Creases on the Surfaces of Elastomers and Gels," Appl. Phys. Lett., **95**(11), p. 111901.
[18] Hohlfeld, E., and Mahadevan, L., 2011, "Unfolding the Sulcus," Phys. Rev. Lett., **106**(10), p. 105702.
[19] Hohlfeld, E., and Mahadevan, L., 2012, "Scale and Nature of Sulcification Patterns," Phys. Rev. Lett., **109**(2), p. 025701.
[20] Gent, A. N., and Cho, I. S., 1999, "Surface Instabilities in Compressed or Bent Rubber Blocks," Rubber Chem. Technol., **72**(2), pp. 253–262.
[21] Brau, F., Vandeparre, H., Sabbah, A., Poulard, C., Boudaoud, A., and Damman, P., 2010, "Multiple-Length-Scale Elastic Instability Mimics Parametric Resonance of Nonlinear Oscillators," Nat. Phys., **7**(1), pp. 56–60.
[22] Brau, F., Damman, P., Diamant, H., and Witten, T. A., 2013, "Wrinkle to Fold Transition: Influence of the Substrate Response," Soft Matter, **9**(34), pp. 8177–8186.
[23] Budday, S., Kuhl, E., and Hutchinson, J. W., 2015, "Period-Doubling and Period-Tripling in Growing Bilayered Systems," Philos. Mag. (Abingdon), **95**(28–30), pp. 3208–3224.
[24] Zang, J., Zhao, X., Cao, Y., and Hutchinson, J. W., 2012, "Localized Ridge Wrinkling of Stiff Films on Compliant Substrates," J. Mech. Phys. Solids, **60**(7), pp. 1265–1279.
[25] Jin, L., Takei, A., and Hutchinson, J. W., 2015, "Mechanics of Wrinkle/Ridge Transitions in Thin Film/Substrate Systems," J. Mech. Phys. Solids, **81**, pp. 22–40.
[26] Mei, H., Landis, C. M., and Huang, R., 2011, "Concomitant Wrinkling and Buckle-Delamination of Elastic Thin Films on Compliant Substrates," Mech. Mater., **43**(11), pp. 627–642.
[27] Cai, S., Breid, D., Crosby, A. J., Suo, Z., and Hutchinson, J. W., 2011, "Periodic Patterns and Energy States of Buckled Films on Compliant Substrates," J. Mech. Phys. Solids, **59**(5), pp. 1094–1114.
[28] Huang, Z., Hong, W., and Suo, Z., 2004, "Evolution of Wrinkles in Hard Films on Soft Substrates," Phys. Rev. E, **70**(3), p. 030601.
[29] Huang, Z., Hong, W., and Suo, Z., 2005, "Nonlinear Analyses of Wrinkles in a Film Bonded to a Compliant Substrate," J. Mech. Phys. Solids, **53**(9), pp. 2101–2118.
[30] Chen, X., and Hutchinson, J. W., 2004, "Herringbone Buckling Patterns of Compressed Thin Films on Compliant Substrates," ASME J. Appl. Mech., **71**(5), pp. 597–603.
[31] Yin, J., Han, X., Cao, Y., and Lu, C., 2014, "Surface Wrinkling on Polydimethylsiloxane Microspheres Via Wet Surface Chemical Oxidation," Sci. Rep., **4**, p. 5710.
[32] Yan, Z., Han, M., Yang, Y., Nan, K., Luan, H., Luo, Y., Zhang, Y., Huang, Y., and Rogers, J. A., 2016, "Deterministic Assembly of 3D Mesostructures in Advanced Materials Via Compressive Buckling: A Short Review of Recent Progress," Extreme Mech. Lett., **11**, pp. 96–104.

[33] Xu, S., Yan, Z., Jang, K.-I., Huang, W., Fu, H., Kim, J., Wei, Z., Flavin, M., McCracken, J., and Wang, R., 2015, "Assembly of Micro/Nanomaterials Into Complex, Three-Dimensional Architectures by Compressive Buckling," Science, **347**(6218), pp. 154–159.
[34] Lejeune, E., Javili, A., and Linder, C., 2016, "An Algorithmic Approach to Multi-Layer Wrinkling," Extreme Mech. Lett., **7**, pp. 10–17.
[35] Lejeune, E., Javili, A., and Linder, C., 2016, "Understanding Geometric Instabilities in Thin Films Via a Multi-Layer Model," Soft Matter, **12**(3), pp. 806–816.
[36] Efimenko, K., Rackaitis, M., Manias, E., Vaziri, A., Mahadevan, L., and Genzer, J., 2005, "Nested Self-Similar Wrinkling Patterns in Skins," Nat. Mater., **4**(4), pp. 293–297.
[37] Diab, M., Zhang, T., Zhao, R., Gao, H., and Kim, K. S., 2013, "Ruga Mechanics of Creasing: From Instantaneous to Setback Creases," Proc. R. Soc. A: Math., Phys. Eng. Sci., **469**(2157), p. 20120753.
[38] Jin, L., Chen, D., Hayward, R. C., and Suo, Z., 2014, "Creases on the Interface Between Two Soft Materials," Soft Matter, **10**(2), pp. 303–311.
[39] Wang, Q., and Zhao, X., 2014, "Phase Diagrams of Instabilities in Compressed Film-Substrate Systems," ASME J. Appl. Mech., **81**(5), p. 051004.
[40] Wang, Q., and Zhao, X., 2015, "A Three-Dimensional Phase Diagram of Growth-Induced Surface Instabilities," Sci. Rep., **5**(1), p. 8887.
[41] Zhao, R., Zhang, T., Diab, M., Gao, H., and Kim, K. S., 2015, "The Primary Bilayer Ruga-Phase Diagram I: Localizations in Ruga Evolution," Extreme Mech. Lett., **4**, pp. 76–82.
[42] Zhao, R., Diab, M., and Kim, K. S., 2016, "The Primary Bilayer Ruga-Phase Diagram II: Irreversibility in Ruga Evolution," ASME J. Appl. Mech., **83**(9), p. 091004.
[43] Wang, Q., and Zhao, X., 2016, "Beyond Wrinkles: Multimodal Surface Instabilities for Multifunctional Patterning," MRS Bull., **41**(2), pp. 115–122.
[44] Tallinen, T., Chung, J. Y., Biggins, J. S., and Mahadevan, L., 2014, "Gyrification From Constrained Cortical Expansion," Proc. Natl. Acad. Sci. U. S. A., **111**(35), pp. 12667–12672.
[45] Budday, S., Raybaud, C., and Kuhl, E., 2014, "A Mechanical Model Predicts Morphological Abnormalities in the Developing Human Brain," Sci. Rep., **4**, p. 5644.
[46] Jin, L., Cai, S., and Suo, Z., 2011, "Creases in Soft Tissues Generated by Growth," EPL (Europhys. Lett.), **95**(6), p. 64002.
[47] Eskandari, M., Kuschner, W. G., and Kuhl, E., 2015, "Patient-Specific Airway Wall Remodeling in Chronic Lung Disease," Ann. Biomed. Eng., **43**(10), pp. 2538–2551.
[48] Shyer, A. E., Tallinen, T., Nerurkar, N. L., Wei, Z., Gil, E. S., Kaplan, D. L., Tabin, C. J., and Mahadevan, L., 2013, "Villification: How the Gut Gets Its Villi," Science, **342**(6155), pp. 212–218.
[49] Amar, M. B., and Jia, F., 2013, "Anisotropic Growth Shapes Intestinal Tissues During Embryogenesis," Proc. Natl. Acad. Sci., **110**(26), pp. 10525–10530.
[50] Noah, T. K., Donahue, B., and Shroyer, N. F., 2011, "Intestinal Development and Differentiation," Exp. Cell Res., **317**(19), pp. 2702–2710.
[51] Tallinen, T., Chung, J. Y., Rousseau, F., Girard, N., Lefèvre, J., and Mahadevan, L., 2016, "On the Growth and Form of Cortical Convolutions," Nat. Phys., **12**(6), pp. 588–593.
[52] Walton, K. D., Kolterud, Å., Czerwinski, M. J., Bell, M. J., Prakash, A., Kushwaha, J., Grosse, A. S., Schnell, S., and Gumucio, D. L., 2012, "Hedgehog-Responsive Mesenchymal Clusters Direct Patterning and Emergence of Intestinal Villi," Proc. Natl. Acad. Sci., **109**(39), pp. 15817–15822.
[53] Taber, L. A., 1995, "Biomechanics of Growth, Remodeling, and Morphogenesis," ASME Appl. Mech. Rev., **48**(8), pp. 487–545.
[54] Eisenhoffer, G. T., Loftus, P. D., Yoshigi, M., Otsuna, H., Chien, C.-B., Morcos, P. A., and Rosenblatt, J., 2012, "Crowding Induces Live Cell Extrusion to Maintain Homeostatic Cell Numbers in Epithelia," Nature, **484**(7395), pp. 546–549.
[55] Frieboes, H. B., Zheng, X., Sun, C. H., Tromberg, B., Gatenby, R., and Cristini, V., 2006, "An Integrated Computational/Experimental Model of Tumor Invasion," Cancer Res., **66**(3), pp. 1597–1604.
[56] Dervaux, J., Couder, Y., Guedeau-Boudeville, M. A., and Ben Amar, M., 2011, "Shape Transition in Artificial Tumors: From Smooth Buckles to Singular Creases," Phys. Rev. Lett., **107**(1), p. 018103.
[57] Tracqui, P., 2009, "Biophysical Models of Tumour Growth," Rep. Prog. Phys., **72**(5), p. 056701.
[58] Nia, H. T., Liu, H., Seano, G., Datta, M., Jones, D., Rahbari, N., Incio, J., Chauhan, V. P., Jung, K., and Martin, J. D., 2016, "Solid Stress and Elastic Energy as Measures of Tumour Mechanopathology," Nat. Biomed. Eng., **1**(1), p. 0004.
[59] Khang, D. Y., Jiang, H., Huang, Y., and Rogers, J. A., 2006, "A Stretchable Form of Single-Crystal Silicon for High-Performance Electronics on Rubber Substrates," Science, **311**(5758), pp. 208–212.
[60] Wang, Q., Tahir, M., Zang, J., and Zhao, X., 2012, "Dynamic Electrostatic Lithography: Multiscale On-Demand Patterning on Large-Area Curved Surfaces," Adv. Mater., **24**(15), pp. 1947–1951.
[61] Shivapooja, P., Wang, Q., Orihuela, B., Rittschof, D., López, G. P., and Zhao, X., 2013, "Bioinspired Surfaces With Dynamic Topography for Active Control of Biofouling," Adv. Mater., **25**(10), pp. 1430–1434.
[62] Levering, V., Wang, Q., Shivapooja, P., Zhao, X., and López, G. P., 2014, "Soft Robotic Concepts in Catheter Design: An On-Demand Fouling-Release Urinary Catheter," Adv. Healthcare Mater., **3**(10), pp. 1588–1596.
[63] Terwagne, D., Brojan, M., and Reis, P. M., 2014, "Smart Morphable Surfaces for Aerodynamic Drag Control," Adv. Mater., **26**(38), pp. 6608–6611.
[64] Lagrange, R., López Jiménez, F., Terwagne, D., Brojan, M., and Reis, P. M., 2016, "From Wrinkling to Global Buckling of a Ring on a Curved Substrate," J. Mech. Phys. Solids, **89**, pp. 77–95.
[65] Zhu, Y., Luo, X. Y., and Ogden, R. W., 2008, "Asymmetric Bifurcations of Thick-Walled Circular Cylindrical Elastic Tubes Under Axial Loading and External Pressure," Int. J. Solids Struct., **45**(11–12), pp. 3410–3429.
[66] Haughton, D., and Ogden, R., 1979, "Bifurcation of Inflated Circular Cylinders of Elastic Material Under Axial Loading—I. Membrane Theory for Thin-Walled Tubes," J. Mech. Phys. Solids, **27**(3), pp. 179–212.
[67] Moulton, D., and Goriely, A., 2011, "Circumferential Buckling Instability of a Growing Cylindrical Tube," J. Mech. Phys. Solids, **59**(3), pp. 525–537.
[68] Li, B., Cao, Y.-P., Feng, X.-Q., and Gao, H., 2011, "Surface Wrinkling of Mucosa Induced by Volumetric Growth: Theory, Simulation and Experiment," J. Mech. Phys. Solids, **59**(4), pp. 758–774.
[69] Wang, L., Pai, C.-L., Boyce, M. C., and Rutledge, G. C., 2009, "Wrinkled Surface Topographies of Electrospun Polymer Fibers," Appl. Phys. Lett., **94**(15), p. 151916.
[70] Yin, J., Chen, X., and Sheinman, I., 2009, "Anisotropic Buckling Patterns in Spheroidal Film/Substrate Systems and Their Implications in Some Natural and Biological Systems," J. Mech. Phys. Solids, **57**(9), pp. 1470–1484.
[71] Li, B., Jia, F., Cao, Y. P., Feng, X. Q., and Gao, H., 2011, "Surface Wrinkling Patterns on a Core-Shell Soft Sphere," Phys. Rev. Lett., **106**(23), p. 234301.
[72] Goriely, A., and Ben Amar, M., 2005, "Differential Growth and Instability in Elastic Shells," Phys. Rev. Lett., **94**(19), p. 198103.
[73] Diab, M., and Kim, K. S., 2014, "Ruga-Formation Instabilities of a Graded Stiffness Boundary Layer in a Neo-Hookean Solid," Proc. R. Soc. A: Math., Phys. Eng. Sci., **470**(2168), p. 20140218.
[74] Steigmann, D. J., and Ogden, R. W., 1997, "Plane Deformations of Elastic Solids With Intrinsic Boundary Elasticity," Proc. R. Soc. A: Math., Phys. Eng. Sci., **453**(1959), pp. 853–877.
[75] Gasser, T. C., Ogden, R. W., and Holzapfel, G. A., 2006, "Hyperelastic Modelling of Arterial Layers With Distributed Collagen Fibre Orientations," J. R. Soc. Interface, **3**(6), pp. 15–35.
[76] Ogden, R. W., 2008, "On Stress Rates in Solid Mechanics With Application to Elasticity Theory," Math. Proc. Cambridge Philos. Soc., **75**(2), pp. 303–319.
[77] Ciarletta, P., Balbi, V., and Kuhl, E., 2014, "Pattern Selection in Growing Tubular Tissues," Phys. Rev. Lett., **113**(24), p. 248101.
[78] Haughton, D., and Ogden, R., 1979, "Bifurcation of Inflated Circular Cylinders of Elastic Material Under Axial Loading—II. Exact Theory for Thick-Walled Tubes," J. Mech. Phys. Solids, **27**(5–6), pp. 489–512.
[79] Haughton, D. M., and Ogden, R. W., 1978, "On the Incremental Equations in Non-Linear Elasticity—II. Bifurcation of Pressurized Spherical Shells," J. Mech. Phys. Solids, **26**(2), pp. 111–138.